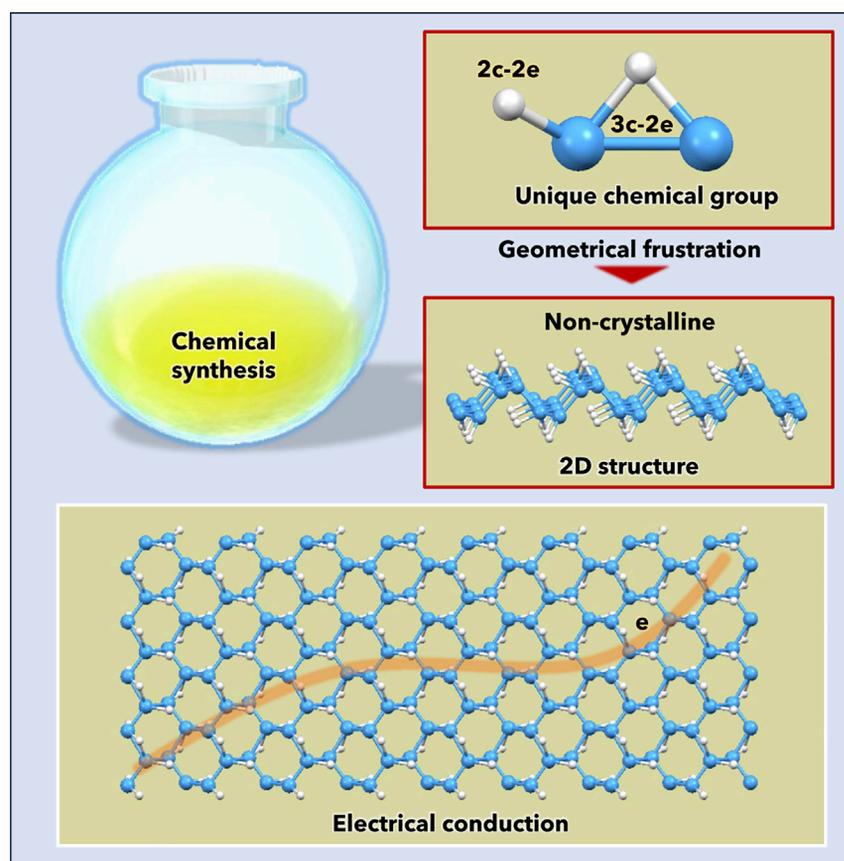# Chem

Article

Geometrical Frustration of B-H Bonds in Layered Hydrogen Borides Accessible by Soft Chemistry

A layered hydrogen boride synthesized via a soft chemical route consists of three-center, two-electron (3c-2e) B-H-B bridging bonds as well as ordinary two-center, two-electron (2c-2e) B-H terminal bonds. The local chemical units form a layered structure, which is amorphous due to the geometrical frustration of terminal B-H bonds. The layered hydrogen boride is electrically conductive.

Satoshi Tominaka, Ryota Ishibiki, Asahi Fujino, ..., Iwao Matsuda, Hideo Hosono, Takahiro Kondo

tominaka.satoshi@nims.go.jp (S.T.)
takahiro@ims.tsukuba.ac.jp (T.K.)

HIGHLIGHTS

The structure of a layered hydrogen boride via a soft chemical route is determined

The structure consists of B-H-B bridging bonds and B-H terminal bonds

The local structure induces macroscopic amorphous nature by geometrical frustration

The layered hydrogen boride is electrically conductive

9 INDUSTRY, INNOVATION AND INFRASTRUCTURE

Article

Geometrical Frustration of B-H Bonds in Layered Hydrogen Borides Accessible by Soft Chemistry

Satoshi Tominaka,[1,2,*] Ryota Ishibiki,[3] Asahi Fujino,[3] Kohsaku Kawakami,[1] Koji Ohara,[2] Takuya Masuda,[4] Iwao Matsuda,[5] Hideo Hosono,[6] and Takahiro Kondo[6,7,8,*]

SUMMARY

Hydrogen borides adopt a variety of structures because of the electron-deficient character of boron. Recently, we reported the synthesis of a layered hydrogen boride via a soft chemical route. Here, we ascertain the atomic arrangements in the layered hydrogen boride by using pair-distribution functions: the material dominantly consists of a corrugated B network decorated with three-center, two-electron B-H-B bridging bonds as well as ordinary two-center, two-electron B-H terminal bonds. The material is locally ordered but amorphous by diffractometry. This discrepancy can be accounted for by geometrical frustration caused by the positions of terminal B-H bonds located on one of two equivalent B atoms in the B-H-B bridging bonds. This material is electrically conductive (0.13 S cm^{-1} below 10°C) rather than ion conductive, and its B-H-B bonds are cleaved by the adsorption of molecules; this dynamic chemical nature originates from the frustrated structure and leads to unique hydrogen boride functionalities.

INTRODUCTION

Boron is an element that is located between metals and non-metals on the periodic table and is known to exhibit intermediate, semimetallic physical properties. Boron has a 2s^{2}2p^1 electronic configuration of valence electrons, which results in as many as 16 bulk allotropes because of the "geometrical frustration" associated with the electron-deficient character of boron.[1–5] This variety of structures originates from electronic configurations that are likely to form molecules or clusters such as B$_{12}$ icosahedra. Boron adopts structures, such as borophene, which is a single-atomic two-dimensional (2D) layer of boron that is analogous to graphene,[6–9] boron nanotubes,[3] which are analogous to carbon nanotubes, and borospherene, which is analogous to fullerene.[10] Some of these boron nanostructures are known to have higher conductivities than those of bulk structures (10^{-4}–10^{-7} S cm^{-1}),[6] for example, boron nanotubes are known to exhibit high metallic conductivities that exceed 10^2 S cm^{-1}.[6]

Carbon allotropes and boron allotropes are to some extent analogous, but their hydrides clearly highlight the differences between boron and carbon. Hydrocarbons are common organic compounds on the Earth and are generally non-conductive because of their fully occupied valence orbitals. Typical boron hydrides are discrete molecules (boranes), such as diborane (B$_2$H$_6$) and decaborane (B$_{10}$H$_{14}$), or anions, such as borohydride (BH$_4^-$). These molecular boranes have been synthesized and investigated for decades, whereas solid-state boron hydrides with extended structures have been investigated little, although they are expected to be conductive

The Bigger Picture

Layered hydrogen borides were investigated computationally, and a variety of structures have been proposed. Although those simulated energetically favored structures are crystalline, the synthesized material is amorphous. Is there any science behind the amorphous nature? Or, is the material simply disordered? Thus, we analyzed the structure fully. The structure consists of three-center, two-electron (3c-2e) B-H-B bridging bonds as well as ordinary two-center, two-electron (2c-2e) B-H terminal bonds. This unique local structure forms a layered structure without long-range orders because of geometrical frustration of terminal B-H bonds. The local structure dominates not only the macroscopic structure but also the electrical conductivity upon adsorption of molecules. Such a dynamic chemical nature is unique as a two-dimensional material and will position hydrogen boride nanosheets as potential sensing materials and catalysts.

because of the electron-deficient nature of boron. In these years, computational studies suggested that some 2D hydrogen borides (HBs) should exhibit unique electronic properties (as summarized in Figures S1–S7).[11–15] Because of the electronic configuration of boron, a variety of 2D boron hydride structures are energetically favorable, as corroborated computationally (cf. Table S1).[11] Because of the fickleness of boron, existing syntheses of 2D boron hydrides do not provide homogeneous and highly pure materials, especially when chemical routes are used.

In 2017, we successfully synthesized one such 2D material in its powder form by the chemical ion exchange of magnesium (Mg) cations in magnesium diboride (MgB_2) for protons in an organic solvent.[16] Through careful analysis, we concluded that the hexagonal boron networks of the original MgB_2 were retained, and proton exchange provided a hexagonal HB (h-HB) structure (cf. Figure S1).[17] Note that this material is referred to as "boride" (rather than a "hydride") because the electronic states of its boron atoms are similar to those in MgB_2.[16] In slightly more detail, this h-HB has a H/B ratio of 1.0 and a layered structure with 6-fold local symmetry and three-center, two-electron (3c-2e) B-H-B bridging bonds. The material is amorphous by X-ray diffractometry (XRD) and exhibits short-range orders of within 6 Å; hence, we considered that the 2-fold symmetry of the hydrogen positions might result in the formation of domains with three different orientations in the 6-fold symmetry of the boron network. Although we proposed a structural model that accounted for the experimental data, the details were not sufficiently clear because of slight oxidization of the sample prepared using our early synthetic method. Moreover, we were concerned that the structure might have changed by oxidation. Such soft chemical methods can produce metastable structures that are often not predicted computationally, and the observed structure might have formed through oxidation of such a metastable structure. Thus, the synthesis and analysis of the unoxidized layered HB is of great importance for achieving a better understanding of this system.

Here, we ascertain the structure of chemically synthesized layered HB and discuss how local ordering on the basis of chemical bond formation results in macroscopic disorder. We found that geometrical frustration accounts for the amorphous state of the layered HB and refer to this structure as "frustrated hydrogen boride" (f-HB). To determine the structure, we improved our Schlenk method and obtained a pure HB sample by a proton-exchange reaction in which MgB_2 crystals were immersed in a methanol (or acetonitrile) solution containing a sulfonated polystyrene as a proton-exchange polymer, under N_2, as reported previously (details are provided in the Supplemental Information, Figures S8 and S9).[16] The structure was fully analyzed using pair-distribution functions (PDFs), XRD, infrared spectroscopy, and quantum chemical calculations. The structure itself is very interesting in view of its geometrical frustration, which tends to form amorphous products. We also investigated the electrical conductivity of the HB sample.

RESULTS AND DISCUSSION

Chemical Synthesis of Oxide-free HB

Black MgB_2 powder was treated by a proton-exchange process. The color of the material changed from black to yellow during the 3-day ion-exchange treatment, and a pale-yellow powder was recovered (Figure 1A). The HB sample was subjected to scanning electron microscopy, as shown in Figure 1A. The HB sample forms sheets, some of which are folded and wrinkled, which indicates that these sheets are flexible. We further evaluated the thickness of the HB sample by atomic force microscopy (AFM) under Ar

[1]International Center for Materials Nanoarchitectonics, National Institute for Materials Science, Tsukuba, Ibaraki 305-0044, Japan

[2]Research and Utilization Division, Japan Synchrotron Radiation Research Institute, 1-1-1 Kouto, Sayo-gun, Hyogo 679-5198, Japan

[3]Graduate School of Pure and Applied Sciences, University of Tsukuba, Tsukuba, Ibaraki 305-8573, Japan

[4]Research Center for Advanced Measurement and Characterization, National Institute for Materials Science, Tsukuba, Ibaraki 305-0044, Japan

[5]Institute for Solid State Physics, University of Tokyo, Kashiwa, Chiba 277-8581, Japan

[6]Materials Research Center for Element Strategy, Tokyo Institute of Technology, Yokohama, Kanagawa 226-8503, Japan

[7]Department of Materials Science and Tsukuba Research Center for Energy Materials Science, Faculty of Pure and Applied Sciences, University of Tsukuba, Tsukuba, Ibaraki 305-8573, Japan

[8]Lead Contact

*Correspondence:
tominaka.satoshi@nims.go.jp (S.T.),
takahiro@ims.tsukuba.ac.jp (T.K.)
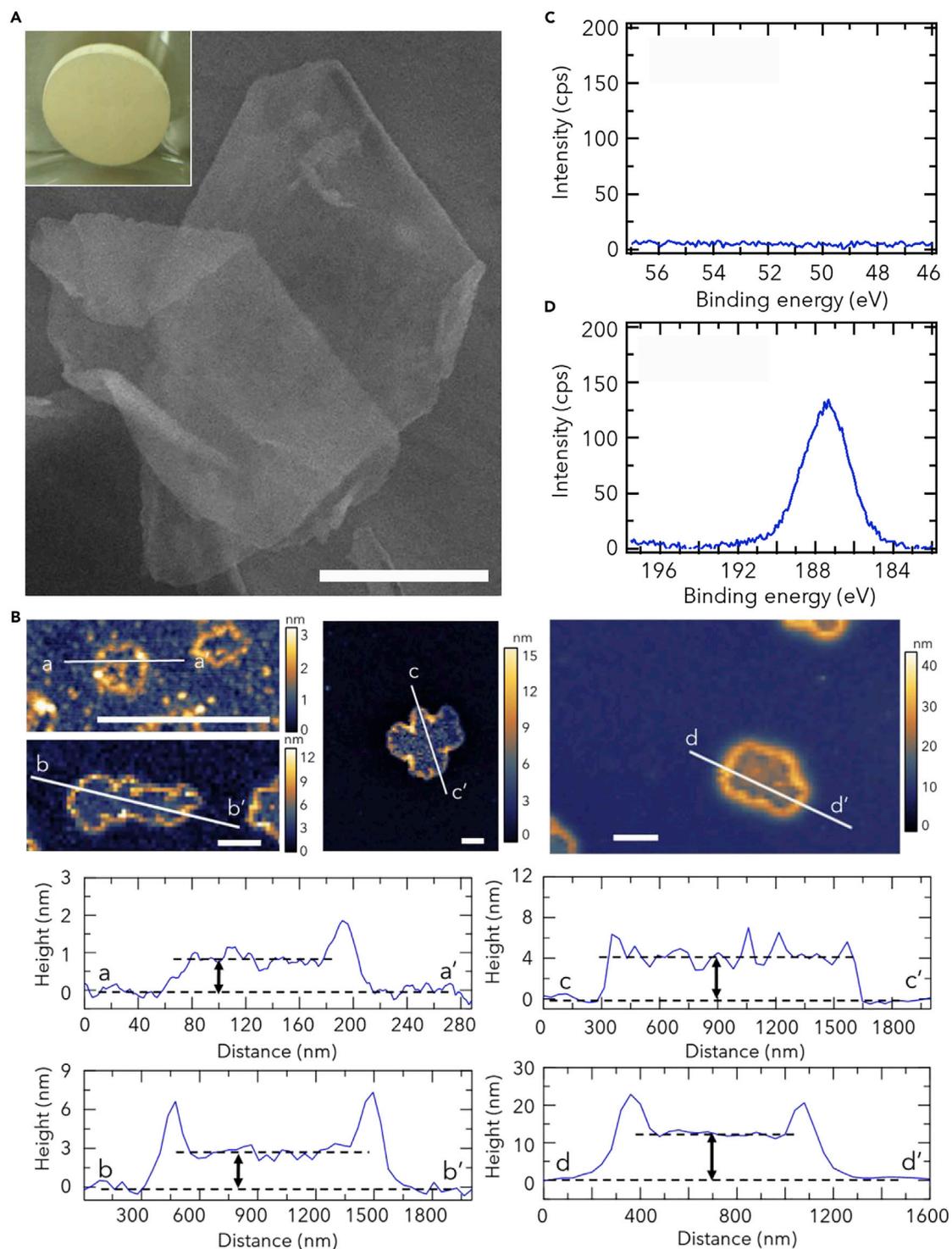https://doi.org/10.1016/j.chempr.2019.11.006

Figure 1. HB Sheets Synthesized by Our Improved Method

(A) Scanning electron microscopy image. Scale bar, 10 μm. The inset shows a photographic image of an HB sample pelletized for conductivity experiments.

(B) AFM images with line profiles for HB on a mica surface. Scale bar, 0.4 μm.

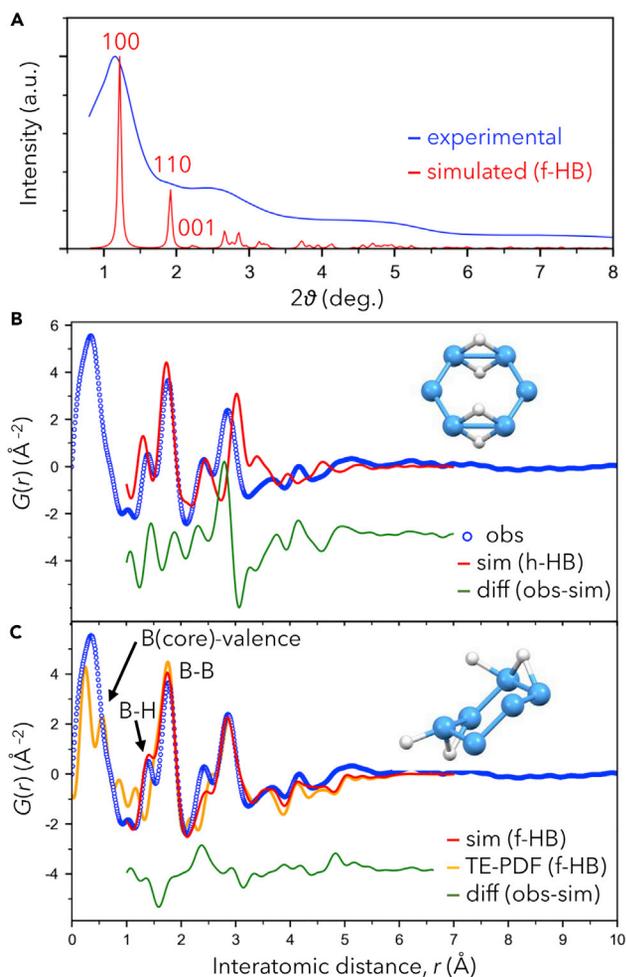(C and D) Core-level Mg 2p (C) and B 1s X-ray photoelectron spectra (D).

Figure 2. Structural Analysis of the Soft Chemically Synthesized Layered HB

(A) X-ray diffraction pattern with the simulated pattern for f-HB.

(B and C) X-ray pair-distribution functions collected at 6°C with those simulated for h-HB (B) and f-HB (C). The yellow curve in the bottom panel is the total-electron PDF simulated for charge densities above 0.8 electrons per $Å^3$, which corresponds to the charge density maps shown in Figure 4. The insets show the primary components that form layered HB structures: B6 hexagonal rings (B: blue balls) and H atoms (white balls).

without exposing the sample to air (Figure 1B). Here, to evaluate its non-aggregated structure, HB sheets were prepared on a mica surface by dropping an acetonitrile suspension, followed by spin coating and drying in a glove box. We found that thinner (~1 nm) and smaller sheets were located at the rotational center of the spin-coated surface (Figure 1B). The thickness corresponds to a few monolayers of HB sheets. Note that thicker (≥ 3 nm) and larger sheets were found at surrounding regions with increasing distance from the rotational center of the spin-coated surface (Figure 1B).

Elemental analysis indicated that H/B = 1.0, and no other elements, including Mg, were detected (Figure S10), as reported previously.[16] The improved synthesis method and purity of the product were also confirmed by the core-level Mg 2p and B 1s photoelectron spectra (Figures 1C and 1D), which show only a single peak for negatively charged boron at 187.5 eV and no oxide component. The absence of an oxidized phase was also confirmed by synchrotron powder XRD, in which Bragg peaks assigned to boric acid crystals were absent (Figure 2A).

Chemical Bonds in the Layered HB

The material is non-crystalline, as evidenced by XRD, which exhibited a broad diffraction pattern (Figure 2A); the non-crystallinity was also confirmed by the X-ray PDF of the material (Figure 2B), which clearly reveals only short-range orders that are within ~6 Å. The fact that the product is amorphous does not mean that the material has no order. We uncovered details, from chemical bonds to overall structures, in a step-by-step fashion. PDFs were obtained from X-ray total scattering experiments (Figure S11) and are useful for discussing bond distances and atomic arrangements. Note that the PDF obtained for this oxide-free sample is different to the one reported previously.[16] The previously reported data were calculated by subtracting the total scattering signal of the more-oxidized sample from that of the less-oxidized sample; the data shown in Figure 2B are without such subtraction treatment. Thus, the unoxidized phase in the previously analyzed sample might have a slightly different and/or non-dominant structure in the sample. Consequently, here, we carefully analyzed the unoxidized phase by using the data obtained for the pure sample.

The main PDF peak (blue dots in Figure 2B) is assigned to the B-B distance, at 1.79 Å (second peak), which is longer than a typical B-B single bond (1.70 Å)[18] and close to that in MgB_2 (1.78 Å, Inorganic Crystal Structure Database [ICSD] no. 93925).[19] This bond length is also close to that in B_2H_6 (1.75–1.79 Å, ICSD no. 15598)[20,21] or other B_2H_6 derivatives with B-H-B bonds (1.82 Å),[22] supporting the formation of 3c-2e bridging bonds at least partially with little stress in terms of B-B bond distances. The peak, located at 1.40 Å, is assigned to a B-H distance and is far longer than a terminal B-H bond (1.18 Å, bond order = 1),[21] which also indicates that layered HB is composed of 3c-2e bridging B-H-B bonds (>1.3 Å, bond order = 0.5) (Figure 2B). When looking at the computationally studied layered HB structures and their simulated PDFs (Figures S1–S7), the formation of 3c-2e bridging bonds is reasonable because the B-H/B-B atomic-pair ratio (namely the ratio of the first PDF peak at around 1.3 Å to the second at around 1.7 Å) of the experimental PDF (Figure 2B) is apparently larger than those in structures devoid of 3c-2e bridging bonds; this is further discussed below together with curve-fitting data.

The Fourier transform infrared (FTIR) spectrum confirms the presence of B-H-B bridging bonds, as evidenced by the presence of a broad peak at around 1,400 cm^{-1} (Figures 3A and 3C) (details of infrared [IR] peak assignments are available in the Supplemental Information, Figures S12–S14). The position of this IR peak is dependent on the B-B distance in the bridging bond (Figure S14) of the hexagonal boron network, and the peak position is well matched to the B-B distance (1.79 nm) obtained by PDF analysis. The additional peak at 2,500 cm^{-1} is assigned to terminal B-H stretching; however, as discussed above, the PDF does not exhibit a peak assigned to typical terminal B-H groups (1.18 Å). Thus, we conclude that the terminal B-H groups are in unique environments, which is further discussed below. In addition to these terminal B-H groups, there is broad absorption behavior above >3,000 cm^{-1}, which is probably assignable to water impurity. Note that this HB material reacted little with water in our hydrolysis experiments. The details of this observed stability to hydrolysis will be reported in the future, but this stability is consistent with the fact that boric acid (oxidized B) was not detected by FTIR spectroscopy, and no oxidized boron was detected by photoelectron spectroscopy.

Local Geometric Frustration Dominates the Macroscopic Amorphous Nature of f-HB

The HB structure was further analyzed by curve fitting the PDF data. The h-HB structure (Figure 2B, top and Figure S1) was chosen as the initial structural model because
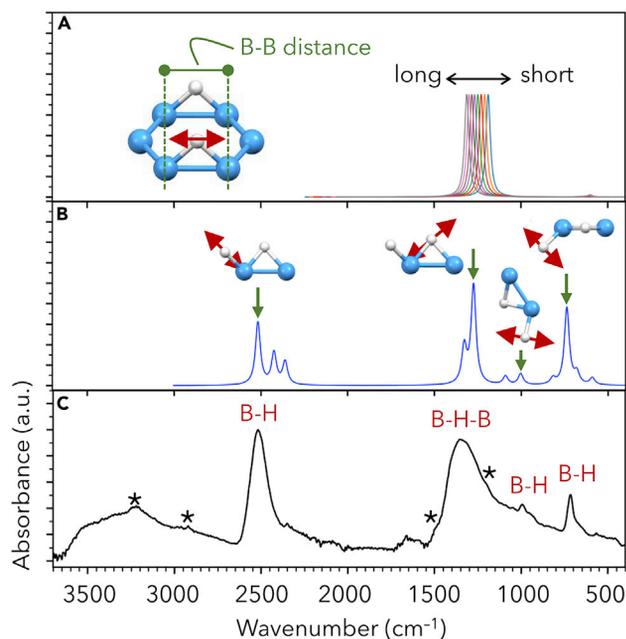
Figure 3. Functional Groups in f-HB as Analyzed by FTIR Spectroscopy

(A) B-H-B vibrations in the bridging bonds in hexagonal B networks are found at around 1,300 cm^{-1} by quantum chemical calculations. The peak positions depend on the B-B distances in the bridging bonds (1.65, 1.68, 1.75, 1.78, 1.79, 1.83, 1.86, and 1.90 Å, from right to left).

(B) Simulated IR spectrum for the f-HB structure solved by PDF analysis. The wavenumbers have been multiplied by 1.13.[23] The insets highlight the major vibrational modes.

(C) Attenuated total reflectance FTIR spectrum (experimental data). The asterisks indicate peaks assigned to boric acid (according to a National Institute of Standards and Technology database).

it contains hexagonal B networks and B-H-B bridging bonds, both of which were determined to exist in the synthesized sample. The initial model was gradually altered by changing the atomic coordinates under the bond-length constraints by least-squares or Bayesian optimization in order to obtain PDF data that resembled the experimental data; both optimization methods resulted in the same atomic arrangement via an in-house program (details are available in the Supplemental Information, Figures S15 and S16). A unit cell model with a = 5.164 Å, b = 4.147 Å, c = 2.843 Å, and β = 103.3° ($P2_1$ space group) accounts for the experimental PDF (Figure 2C, red curve) and FTIR (Figure 3B) data well, with the exception of the amorphous nature shown by XRD (Figure 2A). The formation energy calculated by quantum chemical calculations is −4.48 eV per atom (structure obtained from PDF analysis without geometry optimization, Table S2), which is slightly (by ~0.5 eV per atom) smaller than those of typical layered HBs (Table S1, calculated using norm-conserving pseudopotentials with dispersion corrections). The derived structural model of f-HB is displayed in Figure 4.

The HB structure is composed of corrugated layers of B atoms (Figure 4C) that are formed by hexagonal boron networks of chair-type B6 rings, which means that the original hexagonal boron network of MgB$_2$ has been retained. These chair-type B6 rings are reasonable because the PDF peaks simulated using the h-HB structure (Figure 2B, top), in which the B6 rings are flat, do not match the experimental data at longer distances. B-H-B bridging bonds are located at the ridge lines of the corrugated layers. As opposed to the B$_2$H$_6$-type double B-H-B bridging bonds found in the h-HB model, this structure has a single B-H-B bridging bond per B$_2$ unit, which
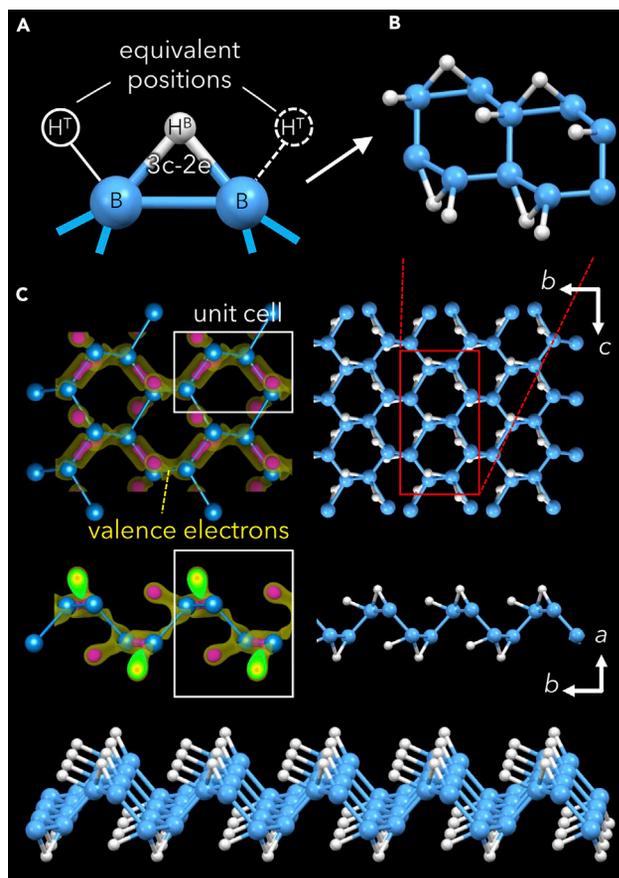
Figure 4. Structural Model of f-HB

(A) Primary unit structure composed of a B-H-B three-center, two-electron (3c-2e) bridging bond. Additional H atoms can be located at two possible terminal positions (H^T) as well as the bridge site (H^B).

(B) The bridging bonds decorate ridge lines of the hexagonal boron network composed of chair-type B6 rings. The terminal B-H bonds are located on the left-hand side in this model.

(C) Corrugated networks shown along different directions. The color maps (left) are charge density maps (valence electrons only) simulated by quantum chemical calculations. The isosurfaces show charge densities at 0.8 (yellow) and 1.2 (red) electrons per $Å^3$, as illustrated using the VESTA program.[24] The blue and white balls show the core positions of B and H atoms, respectively.

is probably due to the step-by-step hydrogenation during the ion-exchange process to form a single B-H-B bridging bond first, which corrugates the B hexagonal layer and then blocks the formation of other B-H-B bridging bonds by steric hindrance.

This bridging bonds are themselves symmetric (B-H^B-B environments, $C2v$ point group; Figure 4A), but the remaining electron per B_2 unit forms a terminal B-H group at one of the equivalent terminal positions (H^T in Figure 4A), resulting in asymmetric B-H^B-B-H^T or H^T-B-H^B-B environments (Cs point group, Figure 4B). As discussed above, this terminal B-H bond is longer than typical B-H bonds (i.e., both B-H bonds in H^T-B-H^B show a peak at around 1.4 Å in Figure 2B), suggestive of weak bonding between the B and H atoms. To discuss the nature of this chemical bonding, we performed Bader charge analysis to understand the partial charges on the various atoms. This charge analysis (Table S3) revealed that the H atoms are negatively charged (partial charges of −0.66 (H^T) and −1.38 (H^B)), whereas the B atoms are positively charged. Bader analysis (Figure S17) also showed that the charges in the B-B

bonds are distributed equally between the B atoms (i.e., indicative of covalent bonding), whereas the charges in the B-H bonds peak around the H cores, and the electrons were distributed along the bonds toward the B atoms (i.e., indicative of covalent bonding with ionic bonding nature). The terminal B-H groups might be expected to provide ionic conduction; however, these H atoms are not macroscopically mobile (electronic conduction appears to dominate over ionic conduction) as observed by AC impedance spectroscopy (below).

The structure is in the $P2_1$ space group, which implies an ordered arrangement of terminal B-H groups, but the lack of long-range ordering indicates disorders in the arrangements of terminal B-H groups. The different B-H arrangements (B-H^B-B-H^T and H^T-B-H^B-B) are equivalent but result in different local distortions of the B layer. Thus, we conclude that the non-crystalline nature of the material originates from such arrangements of H atoms, i.e., the geometrical frustration of terminal B-H groups. This, in turn, means that the local chemical nature of the terminal B-H moiety governs the macroscopic structural and chemical order.

Delocalized Electrons in f-HB Enable Electrical Conduction

Boron has the [He]$2s^2 2p^1$ electronic configuration, and its proportion of valence electrons is significant and detectable by X-ray scattering. The broad feature below 1 Å in the PDF of HB is not due to termination rippling (i.e., noise resulting from the Fourier transformation), rather it is associated with valence-electron scattering.[25] To confirm this, we first calculated the valence-electron charge density (Figure 4C) in the f-HB structure and then simulated the PDF by using the results from these calculations. For this total-electron PDF (TE-PDF) simulation, we used the in-house program described in the Supplemental Information (Figures S18 and S19).

The simulation clearly reproduces the feature below 1 Å (Figure 2C, yellow curve). The peak is mainly associated with pairs of core electrons on B atoms and the valence electrons. The feature at around 0.7 Å is mainly associated with scattering pairs of B core electrons and electrons along the B-B bonds. The TE-PDF does not show a clear peak assigned to the B-H distance, which should be located at around 1.4 Å, as shown by the blue curve, suggesting that electron delocalization around the H atoms has been overestimated in the quantum chemical calculations. Because these calculations implicitly assume a ground state for the crystalline domain using periodic boundary conditions, the calculations might overestimate electron delocalization. This, in turn, suggests that the material is in a metastable state, as also indicated by the observation that PDFs for the structures optimized by quantum chemical calculations do not fit the experimental data well (Figure S19).

Although electron delocalization might be overestimated, the zero band gap (Figure S20) obtained by the quantum chemical calculations for the structure determined by the PDF fitting motivated us to evaluate its conductivity. We acquired AC impedance spectra of f-HB in order to discuss its electronic and/or ionic conductivities and to support the electronic structure described above. A powder sample was pelletized under Ar in a glovebox and then mounted in an airtight cell. Figure 5A displays representative raw impedance data that exhibit behavior typical of an electronic conductor, rather than that of an ionic conductor given that the phase angles are ~0° over the entire frequency range (Figures S21–S24). We also confirmed electrical conduction by acquiring current-voltage curves (Figures 5B and S25), which show ohmic behavior over the entire temperature range (from 0°C to 50°C). This, in turn, means that ionic conduction is, at most, lower than electron conduction and therefore not observable.
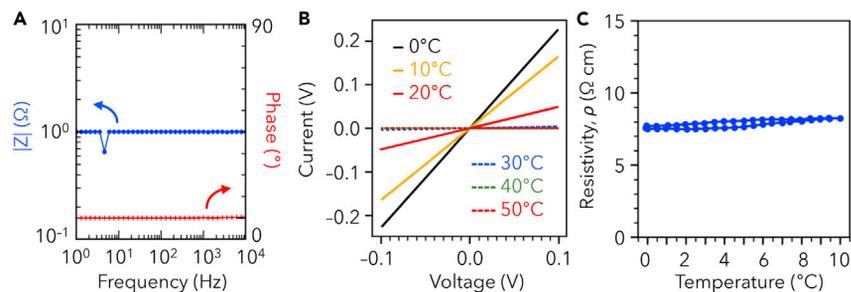
Figure 5. Conductivity of f-HB

(A) AC impedance spectrum acquired at 10°C. The spike at 50 Hz is AC noise.

(B) Current-voltage curves acquired at various temperatures between 0°C and 50°C.

(C) Temperature-dependent resistivity obtained from temperature-controlled AC impedance measurements.

Figure 5C shows the temperature-dependent conductivity of the sample (obtained by impedance spectroscopy). At temperatures below 10°C (Figure 5C), the conductivity is fascinatingly high for an HB, at 0.13 S cm^{-1} (0°C–10°C). The activation energy for conduction was calculated to be −0.10 eV (Figure S24), which indicates that conduction is metallic rather than semiconductive in nature. Metallic conductivity is rare in 2D materials, and only a few compounds such as some of the transition-metal dichalcogenides[26,27] and 2D metal-organic frameworks[28] are known. Our observation is consistent with the zero band gap simulated by quantum chemical calculations for the derived f-HB (Figure S20).

Local Chemistry Governs the Macroscopic Nature

The last part of this paper focuses on the chemical nature of f-HB. We observed a dramatic increase in resistance above 30°C during our conductivity experiments (Figures S21 and S25). This metal-to-insulator transition is found to be reversible, displays an obvious hysteresis, and is reproducible among different samples. It is noteworthy that the impedance phase is still ∼0° at 1 Hz (Figure S22). This phenomenon is not associated with our experimental setup, including electrode contact, as confirmed by control experiments using an Au pellet (Figure S23). The transition was still observed (Figure S21) after the f-HB pellet was heated at 150°C, where weakly bound hydrogen atoms are removed (Figure S26). Hence, the transition is not caused by dehydrogenation.

Temperature-modulated differential scanning calorimetry (DSC) (Figure S27) was used to obtain an understanding of the mechanism associated with the observed dramatic change in impedance; however, this technique did not reveal any peaks or prominent baseline shifts in the relevant temperature range, indicating that the impendence transition is not accompanied by a phase transition, in which enthalpy, entropy, and heat capacity changes. Temperature-controlled FTIR spectroscopy (Figure S12), XRD (Figure S28), XPS, and solid-state NMR spectroscopy failed to detect any obvious changes in the layered HB structure. Temperature-controlled PDFs reveal that peaks assignable to B-H and B-B distances are sharper and more intense at the elevated temperature (Figure S11), whereas the broad feature assignable to the valence electrons located below 1 Å is slightly less intense, which means that electrons are localized around atomic cores at the elevated temperatures.

A similar transition without an obvious structural change was observed in a 2D cobalt dithiolene metal-organic framework, which exhibits a transition to a metallic state at lower temperatures that is probably associated with interlayer states.[28] To investigate the impact of interlayer states, we exposed the HB material to ethanol, which

decreased the intensity of the IR peak assigned to the B-H-B bonds and increased the intensity of the terminal B-H stretching peak (Figure S29). This suggests that the B-H-B bonds dissociate to form terminal B-H bonds by the adsorption of ethanol, which in turn means that the chemical groups in f-HB are flexible and/or dynamic and respond to chemical adsorption.

Careful inspection of the conductivity data reveal that conductivity as well as transition temperature depends slightly on the sample (Figure S21) (note that more samples were measured than shown here) and that residual solvent used in the chemical synthesis is considered to have an impact. Temperature cycling and reassembly of the cell successfully removed the transition (Figure S30); thus, we conclude that the reversible transition is associated with desorption and adsorption of impurities. Temperature cycling between 0°C and 50°C (switched every 1 h) for 5 days resulted in the ordering of local structure, as evidenced by the PDFs (Figure S31). The PDF exhibited a peak at 3.0 Å, which is assigned to the second-nearest neighboring B-B distances of the hexagonal B networks or the third-nearest neighboring H^B-B distances, which also resembles the behavior of the simulated PDF well. The overall PDF became more similar to that simulated for the $P2_1$ structure by optimizing the H positions, yet with a non-crystalline nature (Figure S31).

All of these observations indicate that local B-H chemical bonds in f-HB govern its macroscopic structure as well as electronic nature; f-HB is an electrically conductive solid-state material with local functional groups that respond to chemical adsorption, which we believe will open up the unique functionalities of HB materials.

EXPERIMENTAL PROCEDURES

Preparation of HB Sheets

MgB_2 powder (60 mg, 99%, Rare Metallic Co. Ltd., Tokyo, Japan) was added to 200 mL of methanol (99.8%, Wako Pure Chemical Industries Ltd., Osaka, Japan) or acetonitrile (99.5%, Wako PureChemical Industries Ltd., Osaka, Japan), followed by ultrasonication for 30 min. The prepared suspension was then added to a methanol (or acetonitrile) suspension (100 mL) of the ion-exchange resin (30 mL, Amberlite IR120B hydrogen form, Organo Corp., Tokyo, Japan) under nitrogen at room temperature. After stirring at 250 rpm for 3 days, the supernatant, or filtrate after filtration through a 1.0 or 0.2 μm pore filter (Omnipore Membrane Filters, Merck Millipore, Billerica, MA), was evaporated on an oil bath at 343 K under vacuum to yield the product as a yellow powder. Note that methanol was used for the samples shown in this main text (PDF, IR, and conductivity experiments), and acetonitrile was used for some of the samples shown in the Supplemental Information. Both sets of samples adopt the same structure, as confirmed by their PDFs and IR spectra (Figure S12). Because we found that the dynamic structure changed upon ethanol adsorption, trace amounts of residual solvents are likely to be important for reproducibility; accordingly, the information provided herein has been written as carefully as possible.

Conductivity Measurements

The HB powder sample was pelletized into a 1-cm-diameter, ~620-μm-thick disk at 0.31 GPa under Ar and assembled in a stainless steel cell (split test cell, MTI Corporation). The cell was placed in a temperature-controlled chamber (BioChamber LS-5N, Nippon Brower), which operates as a Peltier temperature controller and a Faraday cage for reducing noise. Impedance spectra were obtained by the AC impedance technique (MTZ-35, BioLogic; input impedance = 10 MΩ) in the 10^4–1 Hz frequency range at an AC voltage of 10 mV. The spectrum was collected every 0.5°C in the 0°C–10°C or 0°C–50°C temperature range for several cycles to

confirm data stability. Current-voltage curves were obtained using an electrochemical measurement system (HZ-7000, Hokuto Denko; Input impedance ≥ 1 TΩ) every 1°C in the 0°C–10°C or 0°C–50°C temperature range for several cycles to confirm data stability (30 min per point). As contact materials, we tested SS304 stainless steel plates as well as copper foil (99.96%, 0.1 mm thick, work function = $\sim$4.51 eV) and confirm that identical data were obtained.

X-Ray Structural Analysis

X-ray total scattering data used to generate PDFs were collected using a flat panel detector on the BL08W beamline (λ = 0.10713 Å) at the SPring-8 facility.[29] The samples were sealed in 1.0-mm-diameter Hilgenberg quartz capillaries under Ar. The collected 2D data were converted into scattering patterns by using the PIXIA program (ver. 8.01),[30] in which all pixels were assumed to be cylindrical absorbers; solid angles, penetration depths, and polarization effects were corrected for each pixel. The scattering data were further corrected using the MaterialsPDF program[30] by subtracting Compton scattering intensities and then normalized using scattering form factors calculated for the H_1B_1 composition by using atomic scattering factors. The obtained structure function, $S(Q)$, was converted into the reduced PDF, $G(r)$, by Fourier transformation (the maximum of the moment transfer of scattering particle [Q_{max}] = 20.4 Å^{-1}) with the revised Lorch function (Δ = 0.9).[31] PDFs were simulated using the PDFfit2 program[32] (Q_{max} = 20.0 Å^{-1}, diameter = 30.0 Å, and the isotropic atomic displacement parameter [U_{iso}] = 0.002 Å^2). In these simulations, we simply assumed all the electrons of each atom are localized at the center of the atom, with a distribution simulated using the atomic displacement parameter. PDF simulation under bond-length constraints and without periodic boundary conditions as well as curve fitting with Bayesian optimization were performed using the in-house program detailed in the Supplemental Information. The TE-PDF was simulated for a model containing the calculated charge densities (valence electrons) and core electrons for the B atoms. The scattering factor for an electron was assumed to be 1.0. Because X-ray scattering factors depend on scattering vectors, and fully delocalized electrons are hard to observe in general scattering experiments, we used electron densities above a cutoff value (0.8 electrons per Å^3) and simulated at interatomic distances above 0.2 Å. The unit cell was divided into 72 × 60 × 50 cells.

Quantum Chemical Calculations

Spectroscopic data were simulated using density functional theory (DFT) within the CASTEP program.[33] The generalized gradient approximation (GGA) and the Perdew-Burke-Ernzerhof (PBE) exchange-correlation functional,[34] with norm-conserving pseudopotentials,[35] which are based on the kinetic energy optimization scheme (details are available in the CASTEP manual),[36] and a 720.0 eV energy cutoff were used. This functional was chosen for its ability to closely simulate the experimental IR spectrum of diborane (although only trivial differences exist between the major functionals). The convergence thresholds are energy = 5 × 10^{-6} eV per atom, maximum force = 0.02 eV per Å, and maximum displacement = 0.003 Å. For the dispersion corrections that take van der Waals interactions into consideration, a semiempirical correction method as represented by the Tkatchenko-Scheffler (TS) scheme was used (sR = 0.94 and d = 20.0).[37] In addition to DFT calculations using norm-conserving pseudopotentials (the CASTEP program), we used the Quantum ESPRESSO program (PWscf program)[38] with projector augmented wave (PAW) pseudopotentials (energy cutoff, 25.0 Ry and charge cutoff, 225.0 Ry) and the PBE exchange-correlation functionals.

DATA AND CODE AVAILABILITY

The codes for analyzing PDFs (TE-PDF and Bayesian optimization) will be available from the National Institute for Materials Science (Satoshi Tominaka).

Chem

SUPPLEMENTAL INFORMATION

Supplemental Information can be found online at https://doi.org/10.1016/j.chempr.2019.11.006.

AUTHOR CONTRIBUTIONS

Conceptualization, S.T. and T.K.; Sample Preparation, R.I. and T.K.; Structural Analysis, PDF Simulation & Programming, Conductivity Experiments, Quantum Chemical Calculations, and IR Spectroscopy, S.T.; XPS and Scanning Electron Microscopy, R.I. and T.K.; AFM, T.M., R.I., and T.K.; Calorimetry, S.T. and K.K.; X-Ray Diffraction, S.T. and K.O.; Ethanol Adsorption in IR, A.F. and T.K.; TDS, A.F., H.H., and T.K.; Writing – Draft, S.T. and T.K.; Discussion of Results, S.T., R.I., A.F., K.K., K.O., T.M., I.M., H.H., and T.K.

DECLARATION OF INTERESTS

The authors declare no competing interests.

REFERENCES AND NOTES

1. Oganov, A.R., Chen, J.H., Gatti, C., Ma, Y.Z., Ma, Y.M., Glass, C.W., Liu, Z.X., Yu, T., Kurakevych, O.O., and Solozhenko, V.L. (2009). Ionic high-pressure form of elemental boron. Nature *457*, 863–867.

2. Ogitsu, T., Schwegler, E., and Galli, G. (2013). β-Rhombohedral boron: at the crossroads of the chemistry of boron and the physics of frustration. Chem. Rev. *113*, 3425–3449.

3. Quandt, A., and Boustani, I. (2005). Boron nanotubes. ChemPhysChem *6*, 2001–2008.

4. Sergeeva, A.P., Popov, I.A., Piazza, Z.A., Li, W.L., Romanescu, C., Wang, L.S., and Boldyrev, A.I. (2014). Understanding boron through size-selected clusters: structure, chemical bonding, and fluxionality. Acc. Chem. Res. *47*, 1349–1358.

5. Wang, L.S. (2016). Photoelectron spectroscopy of size-selected boron clusters: from planar structures to borophenes and borospherenes. Int. Rev. Phys. Chem. *35*, 69–142.

6. Kondo, T. (2017). Recent progress in boron nanomaterials. Sci. Technol. Adv. Mater. *18*, 780–804.

7. Mannix, A.J., Zhou, X.F., Kiraly, B., Wood, J.D., Alducin, D., Myers, B.D., Liu, X.L., Fisher, B.L., Santiago, U., Guest, J.R., et al. (2015). Synthesis of borophenes: anisotropic, two-dimensional boron polymorphs. Science *350*, 1513–1516.

8. Piazza, Z.A., Hu, H.S., Li, W.L., Zhao, Y.F., Li, J., and Wang, L.S. (2014). Planar hexagonal B(36) as a potential basis for extended single-atom layer boron sheets. Nat. Commun. *5*, 3113.

9. Li, W.L., Chen, Q., Tian, W.J., Bai, H., Zhao, Y.F., Hu, H.S., Li, J., Zhai, H.J., Li, S.D., and Wang, L.S. (2014). The B_{35} cluster with a double-hexagonal vacancy: a new and more flexible structural motif for borophene. J. Am. Chem. Soc. *136*, 12257–12260.

10. Zhai, H.J., Zhao, Y.F., Li, W.L., Chen, Q., Bai, H., Hu, H.S., Piazza, Z.A., Tian, W.J., Lu, H.G., Wu, Y.B., et al. (2014). Observation of an all-boron fullerene. Nat. Chem. *6*, 727–731.

11. Jiao, Y., Ma, F., Bell, J., Bilic, A., and Du, A. (2016). Two-dimensional boron hydride

sheets: high stability, massless dirac fermions, and excellent mechanical properties. Angew. Chem. Int. Ed. *55*, 10292–10295.

12. Shukla, V., Araujo, R.B., Jena, N.K., and Ahuja, R. (2018). Borophene's tryst with stability: exploring 2D hydrogen boride as an electrode for rechargeable batteries. Phys. Chem. Chem. Phys. *20*, 22008–22016.

13. Mortazavi, B., Makaremi, M., Shahrokhi, M., Raeisi, M., Singh, C.V., Rabczuk, T., and Pereira, L.F.C. (2018). Borophene hydride: a stiff 2D material with high thermal conductivity and attractive optical and electronic properties. Nanoscale *10*, 3759–3768.

14. Makaremi, M., Mortazavi, B., and Singh, C.V. (2018). 2D hydrogenated graphene-like borophene as a high capacity anode material for improved Li/Na ion batteries: a first principles study. Mater. Today Energy *8*, 22–28.

15. Chen, L., Chen, X., Duan, C., Huang, Y., Zhang, Q., and Xiao, B. (2018). Reversible hydrogen storage in pristine and Li decorated 2D boron hydride. Phys. Chem. Chem. Phys. *20*, 30304–30311.

16. Nishino, H., Fujita, T., Cuong, N.T., Tominaka, S., Miyauchi, M., Iimura, S., Hirata, A., Umezawa, N., Okada, S., Nishibori, E., et al. (2017). Formation and characterization of hydrogen boride sheets derived from MgB_2 by cation exchange. J. Am. Chem. Soc. *139*, 13761–13769.

17. Abtew, T.A., Shih, B., Dev, P., Crespi, V.H., and Zhang, P.H. (2011). Prediction of a multicenter-bonded solid boron hydride for hydrogen storage. Phys. Rev. B *83*, 094108.

18. Bauer, S.H. (1942). Structures and physical properties of the hydrides of boron and of their derivatives. Chem. Rev. *31*, 43–75.

19. Lee, S., Mori, H., Masui, T., Eltsev, Y., Yamamoto, A., and Tajima, S. (2001). Growth, structure analysis and anisotropic superconducting properties of MgB_2 single crystals. J. Phys. Soc. Jpn. *70*, 2255–2258.

20. Smith, H.W., and Lipscomb, W.N. (1965). Single-crystal X-ray diffraction study of β-diborane. J. Chem. Phys. *43*, 1060–1064.

21. Price, W.C. (1948). The absorption spectrum of diborane. J. Chem. Phys. *16*, 894–902.

22. Shoji, Y., Matsuo, T., Hashizume, D., Gutmann, M.J., Fueno, H., Tanaka, K., and Tamao, K. (2011). Boron-boron σ-bond formation by two-electron reduction of a H-bridged dimer of monoborane. J. Am. Chem. Soc. *133*, 11058–11061.

23. Merrick, J.P., Moran, D., and Radom, L. (2007). An evaluation of harmonic vibrational frequency scale factors. J. Phys. Chem. A *111*, 11683–11700.

24. Momma, K., and Izumi, F. (2011). VESTA 3 for three-dimensional visualization of crystal, volumetric and morphology data. J. Appl. Crystallogr. *44*, 1272–1276.

25. Lamzin, V.S., Morris, R.J., Dauter, Z., Wilson, K.S., and Teeter, M.M. (1999). Experimental observation of bonding electrons in proteins. J. Biol. Chem. *274*, 20753–20755.

26. Zhang, Z., Niu, J., Yang, P., Gong, Y., Ji, Q., Shi, J., Fang, Q., Jiang, S., Li, H., Zhou, X., et al. (2017). Van der Waals epitaxial growth of 2D metallic vanadium diselenide single crystals and their extra-high electrical conductivity. Adv. Mater. *29*, 1702359.

27. Lin, Y.C., Dumcenco, D.O., Huang, Y.S., and Suenaga, K. (2014). Atomic mechanism of the semiconducting-to-metallic phase transition in single-layered MoS_2. Nat. Nanotechnol. *9*, 391–396.

28. Clough, A.J., Skelton, J.M., Downes, C.A., de la Rosa, A.A., Yoo, J.W., Walsh, A., Melot, B.C., and Marinescu, S.C. (2017). Metallic conductivity in a two-dimensional cobalt dithiolene metal-organic framework. J. Am. Chem. Soc. *139*, 10863–10867.

29. Ohara, K., Tominaka, S., Yamada, H., Takahashi, M., Yamaguchi, H., Utsuno, F., Umeki, T., Yao, A., Nakada, K., Takemoto, M., et al. (2018). Time-resolved pair distribution function analysis of disordered materials on

beamlines BL04B2 and BL08W at SPring-8. J. Synchrotron Radiat. *25*, 1627–1633.

30. Tominaka, S., Yamada, H., Hiroi, S., Kawaguchi, S.I., and Ohara, K. (2018). Lepidocrocite-type titanate formation from isostructural prestructures under hydrothermal reactions: observation by synchrotron X-ray total scattering analyses. ACS Omega *3*, 8874–8881.

31. Soper, A.K., and Barney, E.R. (2011). Extracting the pair distribution function from white-beam X-ray total scattering data. J. Appl. Crystallogr. *44*, 714–726.

32. Farrow, C.L., Juhas, P., Liu, J.W., Bryndin, D., Božin, E.S., Bloch, J., Proffen, T., and Billinge, S.J.L. (2007). PDFfit2 and PDFgui: computer programs for studying nanostructure in crystals. J. Phys. Condens. Matter *19*, 33.

33. Clark, S.J., Segall, M.D., Pickard, C.J., Hasnip, P.J., Probert, M.I.J., Refson, K., and Payne, M.C. (2005). First principles methods using CASTEP. Z. Kristallogr. Cryst. Mater. *220*, 567–570.

34. Perdew, J.P., Burke, K., and Ernzerhof, M. (1996). Generalized gradient approximation made simple. Phys. Rev. Lett. *77*, 3865–3868.

35. Hamann, D.R., Schlüter, M., and Chiang, C. (1979). Norm-conserving pseudopotentials. Phys. Rev. Lett. *43*, 1494–1497.

36. Lin, J.S., Qteish, A., Payne, M.C., and Heine, V.V. (1993). Optimized and transferable nonlocal separable ab initio pseudopotentials. Phys. Rev. B Condens. Matter *43*, 4174–4180.

37. Tkatchenko, A., and Scheffler, M. (2009). Accurate molecular van der Waals interactions from ground-state electron density and free-atom reference data. Phys. Rev. Lett. *102*, 073005.

38. Giannozzi, P., Baroni, S., Bonini, N., Calandra, M., Car, R., Cavazzoni, C., Ceresoli, D., Chiarotti, G.L., Cococcioni, M., Dabo, I., et al. (2009). QUANTUM ESPRESSO: a modular and open-source software project for quantum simulations of materials. J. Phys. Condens. Matter *21*, 395502.